

1 Ethylamine-Driven Amination of Organic Particles: Mechanistic 2 Insights via Key Intermediates Identification

3 Peiqi Liu¹, Jigang Gao¹, Yulong Hu¹, Wenhao Yuan², Zhongyue Zhou², Fei Qi², and Meirong Zeng¹

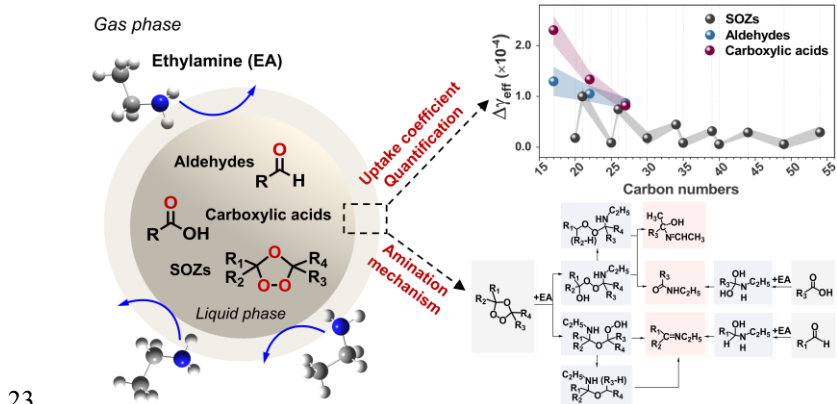
4 ¹College of Smart Energy, Shanghai Jiao Tong University, Shanghai 200240, P.R. China

5 ²School of Mechanical Engineering, Shanghai Jiao Tong University, Shanghai 200240, P.R. China

6 Correspondence to: Meirong Zeng (meirongzeng@sjtu.edu.cn)

7 **Abstract:** Atmospheric amines critically contribute to secondary aerosols formation via heterogeneous reactions, yet the
8 molecular mechanisms governing heterogeneous amination chemistry of aerosols remain unclear. Here, we utilize an
9 integrated tandem flow-tube system coupled with online ultrahigh-resolution mass spectrometry to elucidate the amination
10 chemistry of ethylamine (EA) with representative organic aerosol components, including C₂₀-C₅₄ secondary ozonides (SOZs),
11 C₁₇-C₂₇ carboxylic acids, and aldehydes. Our experiments provide evidence for the formation of four key intermediates:
12 hydroxyl peroxyamines, amino hydroperoxides, peroxyamines, and amino ethers, which mediate SOZs conversion to
13 hydroxyimines, amides, and imines. Furthermore, dihydroxylamines and hydroxylamines are identified as characteristic
14 intermediates in carboxylic acids and aldehydes amination. Quantitative heterogeneous reactivity measurements ($\Delta\gamma_{\text{eff}}$) reveal
15 that SOZs exhibit a pronounced inverse dependence on carbon chain length, e.g., C₂₁ SOZ ($\Delta\gamma_{\text{eff}} = 1.0 \times 10^{-4}$) > C₄₉ SOZ ($\Delta\gamma_{\text{eff}}$
16 = 5.7×10^{-6}), with consistently lower reactivity than acids and aldehydes, e.g., C₁₇ acid ($\Delta\gamma_{\text{eff}} = 2.3 \times 10^{-4}$). The amination
17 mechanism of SOZs is initiated by EA addition, followed by either hydroxyl peroxyamines-mediated dehydration yielding
18 hydroxyimines and amides, or amino hydroperoxides-driven H₂O₂ elimination forming imines. For carboxylic acids and
19 aldehydes, EA addition leads to dihydroxylamines and hydroxylamines formation, which subsequently dehydrate to produce
20 amides and imines. These findings provide a mechanistic framework for understanding amine-driven aerosol aging processes
21 that affects atmospheric chemistry, air quality, and climate systems.

22 Graphic abstracts



24 **1 Introduction**

25 Atmospheric aerosols undergo complex chemical transformations that significantly affect human health, environmental quality, and climate systems (Shen et al., 2023; George and Abbatt, 2010). The heterogeneous evolution of organic aerosols, initiated by gaseous amines, drives the formation and growth of nitrogen-containing secondary organic aerosols (SOAs), which are critical components of atmospheric pollution (Na et al., 2007; De Haan et al., 2011; Tian et al., 2024). These transformations are governed by composition-dependent amination mechanisms, with distinct pathways for different organic aerosols, such as carboxylic acids (RCOOHs), aldehydes (RCHOs), and secondary ozonides (SOZs). Quantitative analysis of multiple amination reactions of these particles provides fundamental insights into the chemical evolution process of atmospheric SOAs. The decomposition of SOZs upon amine exposure is initiated by a nucleophilic attack on the carbon atom of SOZs (Jørgensen and Gross, 2009). However, subsequent reaction pathways remain controversial. Na et al. (2006) demonstrated that the nucleophilic attack of NH₃ on a 3,5-diphenyl-1,2,4-trioxolane (denoted as C₁₄ SOZ), derived from the gas-phase ozonolysis of styrene, induces ring-opening reaction to form a C₁₄ amino hydroperoxide. This crucial intermediate subsequently decomposes to yield H₂O₂, benzaldehyde, and phenylmethanimine (C₇H₇N). Consistently, Almatarneh et al. (2020) and Jørgensen and Gross (2009) identified C₂ amino hydroperoxide intermediates from the reactions of NH₃ with a C₂ SOZ, derived from the ozonolysis of ethene. In contrast, Zahardis et al. (2008) observed that the attack of octadecylamine (ODA, C₁₈H₃₉N) on a C₁₈ SOZ, produced from the ozonolysis of oleic acid, generates a C₃₆ hydroxyl peroxyamine intermediate, ultimately forming H₂O, nonanal, and C₂₇ amide. More recently, Qiu et al. (2024) reported that the attack of ethylamine on a C₁₅ SOZ, derived from the ozonolysis of β-caryophyllene, directly opens the ring and generates H₂O and a C₁₇ amine.

42 To our knowledge, these key intermediates (amino hydroperoxide and hydroxyl peroxyamine) have not been experimentally measured in prior studies (Na et al., 2006; Jørgensen and Gross, 2009; Almatarneh et al., 2020; Zahardis et al., 2008), creating uncertainty about their mechanistic roles in controlling the evolution of SOZ upon amine exposure. The measured stable amination products (amides, imines, and amines) additionally exhibit inconsistency across studies (Na et al., 2006; Jørgensen and Gross, 2009; Almatarneh et al., 2020; Zahardis et al., 2008). Furthermore, previous experimental investigations primarily focused on qualitative products identification, lacking both quantitative reaction rates of SOZ and amine, as well as kinetics analyses of product formation. These factors limit the evaluation of the amination chemistry in the atmosphere. To mimic the heterogeneous reactions of SOZs and amine, we generated SOZ particles via the heterogeneous ozonolysis of alkene, their dominant natural formation pathway (Qiu et al., 2024; Qiu et al., 2022). Specifically, the ozonolysis of squalene (Sqe) was chosen as model system to generate SOZ particles, building on the demonstration of high SOZ yields (maximum ~21% total yield) from Sqe ozonolysis (Heine et al., 2017). Meanwhile, this Sqe ozonolysis system produces some carbonyl byproducts (e.g., aldehydes and carboxylic acids) enabling simultaneous quantification of carbonyl aerosols upon amine exposure. It is widely established that reactions between carboxylic acids and amines typically proceed via acid-base neutralization to form ammonium salts (Na et al., 2007; Liu et al., 2012; Smith et al., 2010; Gao et al., 2018). However, Ditto et al. (2022) demonstrated experimentally that the heterogeneous reaction of oleic acid (C₁₈H₃₄O₂) and NH₃ yields an oleamide (C₁₈H₃₅ON)

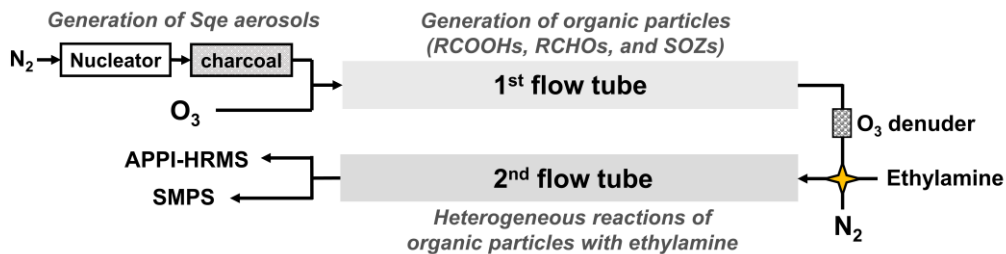
57 and H₂O. This observation aligns with the calculated pathways by Charville et al. (2011), who suggested that the reaction
58 between carboxylic acid and amine generates a dihydroxyamine intermediate that subsequently dehydrates to form an amide.
59 Moreover, significant uncertainties persist regarding the heterogeneous reaction rates of such carboxylic acid and amine
60 reactions (Fairhurst et al., 2017a; Fairhurst et al., 2017b; Liu et al., 2012). Fairhurst et al. (2017a) reported the heterogeneous
61 reaction rates (uptake coefficient, γ) ranging from 10⁻¹ (malonic acid) to 10⁻⁵ (adipic acid) upon ethylamine (C₂H₇N) exposure.
62 They further revealed that the uptake of amines onto low-molecular-weight diacids (C₃-C₈) is structure-dependent, with higher
63 γ values observed for odd-carbon diacids than even-carbon ones. Additionally, γ decreases with increasing carbon chain length
64 of diacids. However, these trends remain unestablished for long-chain acids. Furthermore, to our knowledge, the heterogeneous
65 uptake coefficients for aldehyde particles upon amine exposure have not been experimentally measured.

66 Our objective is to investigate the heterogeneous reactions of particulate SOZs, carboxylic acids, and aldehydes upon exposure
67 to gaseous ethylamine (selected as model amine), using a tandem flowtube reactor. As a representative atmospheric amine
68 (Lee and Wexler, 2013), ethylamine was selected for its remarkable heterogeneous reactivity and simple structure. The
69 atmospheric pressure photoionization high-resolution mass spectrometer (APPI-HRMS) is used to identify reaction products
70 and measure reaction kinetics as a function of ethylamine exposure. Additionally, the heterogeneous uptake coefficients for
71 SOZs, aldehydes, and acids are quantified. To interpret the experimental data, the multiphase reaction mechanisms governing
72 the decomposition of SOZs, carboxylic acids, and aldehydes, as well as the formation of featured amination products are
73 revealed.

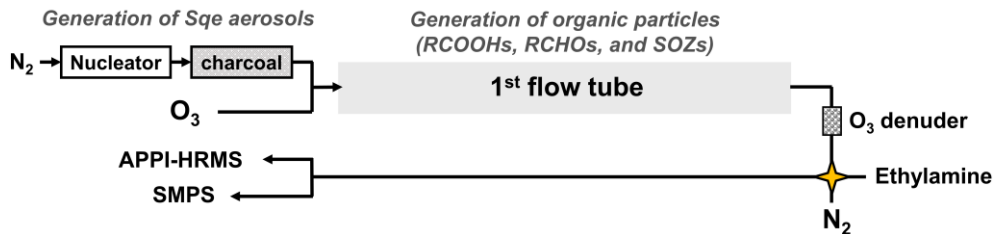
74 **2 Experimental methods**

75 An integrated experimental system employing a tandem flowtube reactor coupled with APPI-HRMS was developed to examine
76 the heterogeneous reactions between target organic aerosols upon ethylamine exposure, as illustrated in Fig. 1a. The apparatus
77 contains three key components: (i) *in-situ* generation of organic particles in the first flowtube reactor from the ozonolysis of
78 S_{qe} aerosols, (ii) controlled multiphase reactions between organic particles and ethylamine in the secondary flowtube reactor,
79 and (iii) online monitoring of chemical compositions of organic particles as a function of ethylamine exposure. To isolate the
80 contribution of heterogeneous reactions in the secondary flowtube reactor (Fig. 1a), the controlled experiments were conducted
81 using a single flowtube configuration, as illustrated in Fig. 1b.

82 (a) Tandem flowtube experiments



84 (b) Controlled one flowtube experiments



86 **Figure 1: Schematic diagrams of (a) the tandem flowtube system, and (b) the controlled one flowtube experiment.**

87 **2.1 Generation of organic particles in the first flowtube reactor**

88 Polydisperse Sqe aerosols were generated via homogeneous nucleation by passing N_2 (300 mL/min) through a Pyrex tube
 89 filled with liquid Sqe (Sigma-Aldrich, 99% purity), located in a tube furnace setting at 145 °C (Fig. 1). Upon exiting the Pyrex
 90 tube, the Sqe vapor cooled and homogeneously nucleated to form aerosols, which were subsequently passed through an annular
 91 activated charcoal denuder to remove any residual gas-phase organics produced in the oven. The average Sqe particle
 92 distribution was log-normal with a mass concentration of 6120 $\mu\text{g}/\text{m}^3$ and an average diameter of 209 nm (Fig. S1).

93 The Sqe aerosol flow was then introduced into the first quartz flowtube reactor (130 cm long and 2.6 cm inner diameter) where
 94 they reacted with O_3 to generate organic particles, mainly composed of SOZs, aldehydes, and carboxylic acids (Heine et al.,
 95 2017). O_3 was generated by passing 20 mL/min O_2 through a corona discharge generator (com-ad-02, Anseros, China), with
 96 its concentration monitored using an O_3 analyzer (GM-6000-OEM, Anseros, China). Dilute dry N_2 (580 mL/min) was also
 97 introduced into the first flowtube reactor to achieve a total flow rate of 900 mL/min, corresponding to an average residence
 98 time of 46 seconds. The O_3 concentration in the first flowtube reactor was varied from 0 to 0.678 ppm.

99 The chemical compositions of organic aerosols generated in the first flowtube reactor were analyzed using APPI-HRMS (Liu
 100 et al., 2024). As illustrated in Figs. S2a and S3a, the major components were identified as SOZs, carboxylic acids, and
 101 aldehydes, consistent with the product distributions measured using vacuum ultraviolet aerosol mass spectrometer (VUV-
 102 AMS) (Heine et al., 2017; Arata et al., 2019). Figure S4 displays the mass signals of representative compounds, including C_{27}
 103 aldehyde ($C_{27}H_{44}O$), C_{22} acid ($C_{22}H_{36}O_2$), and C_{35} SOZ ($C_{35}H_{58}O_3$), as a function of O_3 concentration in the first flowtube
 104 reactor. It is demonstrated that, at fixed O_3 concentration (e.g., 0.57 ppm), the mass signals of these compounds are stable over
 105 30 min-operation periods with little signal fluctuation. The size distribution of organic particles was monitored using a

103 Scanning Mobility Particle Sizer (SMPS, TSI 3080L DMA and 3776 CPC), revealing an average diameter of 201 nm (Fig.
104 S1).

105 **2.2 Reactions of organic particles with ethylamine in the secondary flowtube reactor**

106 Upon exiting the first flowtube reactor and subsequent O₃ denuder, the organic particles were introduced into a secondary
107 quartz flowtube reactor (130 cm long and 2.6 cm inner diameter) to investigate their heterogeneous reactions with ethylamine
108 (Fig. 1a). This coupled reactor configuration, combining organic aerosols generated in the first flowtube reactor with amine
109 exposure in the secondary flowtube, is designated as the tandem 2FT experimental system. Ethylamine was supplied from a
110 standard gas cylinder (1000 ppm ethylamine balanced with nitrogen; Wetry, Shanghai, China). A mixture of organic particle
111 flow, ethylamine, and diluent N₂ was introduced into the secondary flowtube reactor, maintaining a total flow rate of 1100
112 mL/min (corresponding to an average residence time of 37 seconds). The ethylamine concentration in the secondary flowtube
113 reactor was varied from 0 to 43.45 ppm. All experiments were conducted at atmospheric pressure and room temperature. The
114 experiments have been conducted under dry condition, corresponding to a relative humidity of approximately 3% (Heine et
115 al., 2017).

116 **2.3 Controlled experiments in one flowtube reactor**

117 As widely demonstrated (Bos et al., 2006; Fredenhagen and Kuhnol, 2014), the reaction kinetics measured using the APPI
118 technique could be influenced by potential photochemical side reactions (Fig. S5). To eliminate contributions from interactions
119 between ethylamine and organic aerosols in the APPI region, control experiments were designed (Fig. 1b). In these control
120 experiments, organic aerosols generated in the first flowtube reactor were introduced directly into the APPI region, bypassing
121 the secondary flowtube reactor. By subtracting the reaction kinetics of the 1FT controlled experiments from those obtained in
122 the tandem 2FT experiments, the net contribution of heterogeneous reactions occurring in the secondary flowtube reactor was
123 quantitatively determined (Fig. S6).

124 **2.4 Real-time detection system and data analysis for heterogeneous reactions**

125 A portion of the particle stream was sampled by the SMPS to measure particle size distribution and concentration. The
126 remaining flow (800 mL/min) was directed into the ionization region of the APPI-HRMS (Orbitrap Fusion, Thermo Scientific)
127 for real-time chemical characterization (Fig. S5). Additional details on the application of APPI-HRMS for quantifying
128 heterogeneous reactions of particles are available in our previous work (Liu et al., 2024).

129 By monitoring the mass signals of organic particles (denoted as [Particle]) as a function of ethylamine exposure, defined as
130 the concentration of ethylamine ([ethylamine]) \times residence time (*t*), the heterogeneous decay rate (*k_{particle}*) was determined
131 through fitting the decay profiles to an exponential function (Equation 1) (Smith et al., 2009; Liu et al., 2024). The effective
132 uptake coefficient (γ_{eff}), representing the probability of reactive particle decay upon ethylamine collisions, was then calculated
133 using Equation 2 (Liu et al., 2024; Smith et al., 2009). In Equation 2, *D*, ρ_0 , *N_A*, \bar{c} , and *M* correspond to particle diameter,

134 density, Avogadro's number, mean speed of ethylamine, and molar mass of reactant molecules, respectively. In this work, the
 135 heterogeneous reaction rates measured in the 2FT flowtube reactor experiments and single flowtube reactor (1FT) experiments
 136 were designated as $\gamma_{\text{eff, 2FT}}$ and $\gamma_{\text{eff, 1FT}}$, respectively. The net contribution of heterogeneous reactions in the secondary flowtube
 137 reactor was quantified by subtracting $\gamma_{\text{eff, 1FT}}$ from $\gamma_{\text{eff, 2FT}}$, yielding the differential uptake coefficient ($\Delta\gamma_{\text{eff}}$) as defined in
 138 Equation 3. Figure S6 presents the decay kinetics and corresponding $\Delta\gamma_{\text{eff}}$ values for representative compounds: C₂₇ aldehyde,
 139 C₂₇ acid, and C₂₀ SOZ. For instance, $\gamma_{\text{eff, 2FT}}$ and $\gamma_{\text{eff, 1FT}}$ values for C₂₀ SOZ were determined to be 8.0×10^{-5} and 6.2×10^{-5} ,
 140 respectively, resulting in $\Delta\gamma_{\text{eff}} = 1.8 \times 10^{-5}$.

$$141 \frac{[\text{Particle}]}{[\text{Particle}]_0} = \exp(-k_{\text{particle}} \times [\text{Ethylamine}] \times t) \quad (\text{E1})$$

$$142 \gamma_{\text{eff}} = \frac{4 \times k_{\text{particle}} \times D \times \rho_0 \times N_A}{6 \times \bar{c} \times M} \quad (\text{E2})$$

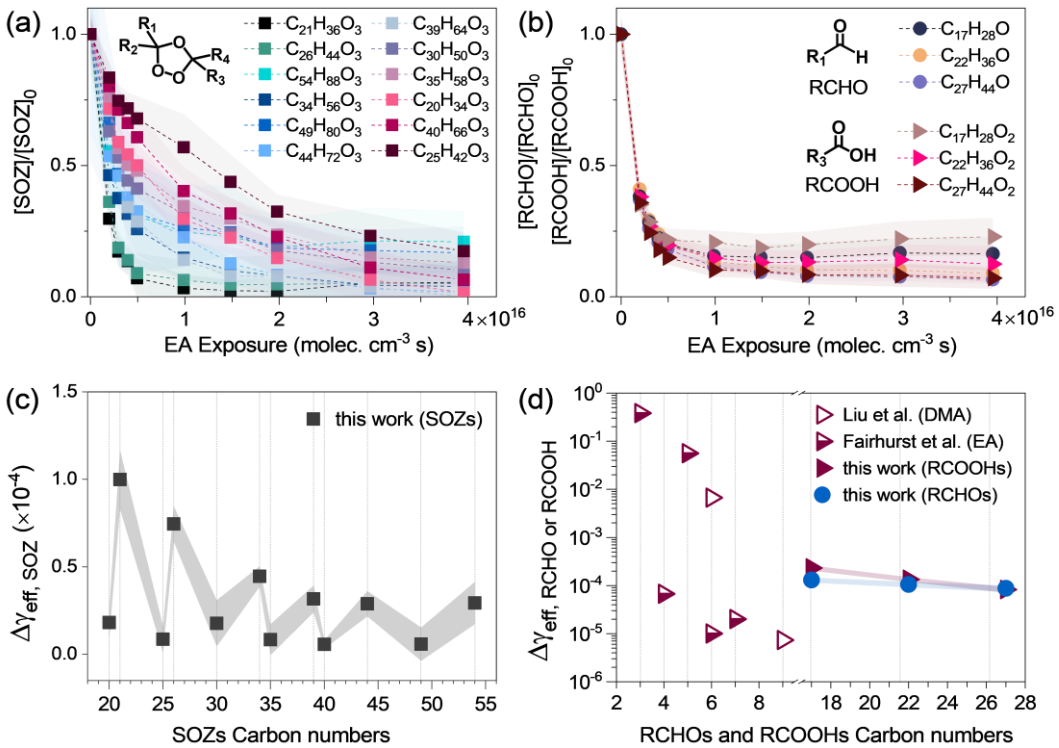
$$143 \Delta\gamma_{\text{eff}} = \gamma_{\text{eff, 2FT}} - \gamma_{\text{eff, 1FT}} \quad (\text{E3})$$

144 3 Results and discussion

145 3.1 Heterogeneous reactions rates of organic aerosols upon ethylamine exposure

146 The O₃ addition reactions to the C=C bonds of Sqe in the first flowtube reactor generate primary ozonides (POZs) (Heine et
 147 al., 2017), as illustrated in Fig. S8. These POZs subsequently decompose to form three ketones (C₃H₆O, C₈H₁₄O, and C₁₃H₂₂O)
 148 with molecular weights (*MWs*) of 58, 126, and 194, three aldehydes (C₁₇H₂₈O, C₂₂H₃₆O, and C₂₇H₄₄O) with *MWs* of 248, 316,
 149 and 384, and six Criegee intermediates (CIs) (Heine et al., 2017). Unimolecular isomerization reactions of C₁₇, C₂₂, and C₂₇
 150 CIs produce carboxylic acids (C₁₇H₂₈O₂, C₂₂H₃₆O₂, and C₂₇H₄₄O₂) with *MWs* of 264, 332, and 400 (Arata et al., 2019; Zahardis
 151 et al., 2005). Bimolecular reactions between CIs and aldehydes (or ketones) generate a series of SOZs (Fig. S9), including C₆,
 152 C₁₁, C₁₆, C₂₀, C₂₁, C₂₅, C₂₆, C₃₀, C₃₄, C₃₅, C₃₉, C₄₀, C₄₄, C₄₉, and C₅₄ SOZs (Heine et al., 2017). Considering the relative higher
 153 partitioning of smaller species (e.g., ketones and smaller SOZs) into the gas phase, the present work mostly focused on larger
 154 SOZs, aldehydes, and carboxylic acids.

155 Figure 2a illustrates the relative abundance of C₂₀ to C₅₄ SOZs as a function of ethylamine exposure. These SOZs exhibit
 156 distinct heterogeneous decay rates (k_{particle}), with the C₂₁ SOZ exhibiting the highest rate. The differential effective uptake
 157 coefficients ($\Delta\gamma_{\text{eff}}$), quantifying the contribution of SOZ reactions with ethylamine in the secondary flowtube reactor, were
 158 then calculated using Equations E2 and E3 (Fig. 2c and Table S2). The $\Delta\gamma_{\text{eff}}$ values of SOZs generally show consistent
 159 tendencies with the decay kinetics and exhibit a zigzag pattern that decreases with increasing carbon chain length of SOZs.



160
161 **Figure 2: (a-b) Decay of SOZs, aldehydes, and carboxylic acids as a function of ethylamine (EA) exposure in tandem flowtube**
162 **experiments. (c-d) Differential effective uptake coefficients ($\Delta\gamma_{\text{eff}}$) for C_{20} , C_{21} , C_{25} , C_{26} , C_{30} , C_{34} , C_{35} , C_{39} , C_{40} , C_{44} , C_{49} , and C_{54} SOZs; C_{17} , C_{22} , and C_{27} carboxylic acids, and C_{17} , C_{22} , and C_{27} aldehydes. Uptake coefficients for carboxylic acids from Refs.(Liu et al., 163 2012; Fairhurst et al., 2017a) are included.**

165 Differences in the initial concentrations of SOZs may contribute to their distinct heterogeneous reactivities ($\Delta\gamma_{\text{eff}}$) shown in
166 Fig. 2c. As demonstrated by Heine et al. (2017), in multi-component particles, the heterogenous reactivity of each component
167 depends on its initial concentration (Jacobs et al., 2016; Zeng et al., 2020; Arata et al., 2019). Heine et al. (2017) reported that
168 the abundance of SOZs formed during the ozonolysis of squalene varies, following the order: $\text{C}_{30} > \text{C}_{25}$, $\text{C}_{35} > \text{C}_{44} > \text{C}_{20}$, C_{21} ,
169 C_{39} , C_{40} , $\text{C}_{49} > \text{C}_{26}$, C_{34} , C_{54} SOZs, as illustrated in Fig. S7a. Consequently, in this work, the initial concentrations of SOZs
170 formed from the ozonolysis of Sqe in the flowtube reactor differ. To quantify the influence of the initial SOZ concentrations
171 on their heterogeneous reaction rates, the $\Delta\gamma_{\text{eff}}$ values for SOZs were normalized for their corresponding initial concentrations.
172 As illustrated in Fig. S7b, the normalized $\Delta\gamma_{\text{eff}}$ values exhibit smaller differences compared to the original $\Delta\gamma_{\text{eff}}$ values. This
173 observation supports the hypothesis that differences in initial SOZ concentrations affect their decay rate upon ethylamine
174 exposure. Additionally, SOZs with long-chain substituents (e.g., C_{54} SOZ) exhibit lower reactivity (Ponec et al., 1997). This
175 reduced reactivity may be attributed to the steric hindrance effects (Hon et al., 1995), which restrict the conformational
176 flexibility of SOZ molecules during attack by ethylamine.

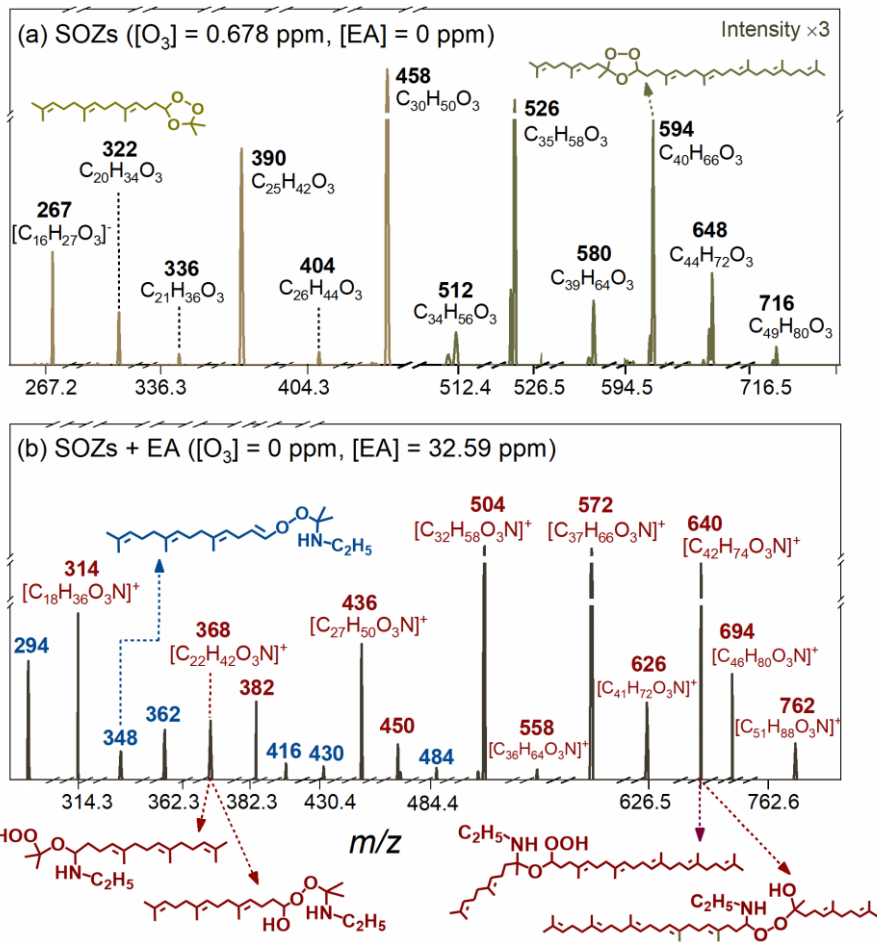
177 Figure 2b illustrates the decay kinetics of representative aldehydes and carboxylic acids. These aldehydes and carboxylic acids
178 decay faster than SOZs. Consistently, their differential effective coefficients ($\Delta\gamma_{\text{eff}}$ from 10^{-5} to 10^{-4}) are larger than

179 those of SOZs (10^{-5} to 10^{-6}), as illustrated in Fig. 2d. This difference could be explained by the higher acidity of carboxylic
180 acids, which enhances the heterogeneous reactions between these acids upon ethylamine exposure. As reported by Liu et al.
181 (2012) the heterogeneous uptake coefficients of dimethylamine (C_2H_7N , an isomer of ethylamine), with citric acid (a triacid,
182 $C_6H_8O_7$, $\gamma \sim 10^{-3}$) is significantly larger than with humic acid (a diacid, $C_9H_9NO_6$, $\gamma \sim 10^{-6}$). They attributed this difference to
183 the stronger acidity of citric acid relative to humic acid.

184 Figure 2d illustrates that the measured $\Delta\gamma_{\text{eff}}$ values for carboxylic acids follow the trend: $C_{17}H_{28}O_2 > C_{22}H_{36}O_2 > C_{27}H_{44}O_2$,
185 indicating a negative dependence of heterogeneous reactivity on carbon chain length. A similar trend is observed for aldehydes,
186 i.e., $C_{17}H_{28}O > C_{22}H_{36}O > C_{27}H_{44}O$. To our knowledge, no prior experimental measurements exist for the heterogeneous
187 reactivity of aldehyde particles with ethylamine, whereas reactivity trends for carboxylic acids of varying carbon chain length
188 have been investigated (Fairhurst et al., 2017a). For example, Fairhurst et al. (2017a) measured the heterogeneous reactivities
189 of ethylamine by solid dicarboxylic acids with varying carbon numbers: malonic acid ($C_3H_4O_4$), succinic acid ($C_4H_6O_4$),
190 glutaric acid ($C_5H_8O_4$), adipic acid ($C_6H_{10}O_4$), and pimelic acid ($C_7H_{12}O_4$). Their measured uptake coefficients are
191 approximately 10^{-1} for C_3 diacids, 7×10^{-5} for C_4 diacid, and 1×10^{-5} for the C_6 diacid. They attributed this trend to differences
192 in the crystalline surface structures of these solid acids. Thus, these reported uptake coefficients for carboxylic acids reacting
193 with amine span a wide range (10^{-1} to 10^{-6}), suggesting that more comprehensive data are needed to elucidate the reactivity
194 trends for both carboxylic acids and aldehydes across varying carbon chain length.

195 3.2 Products distribution during the heterogeneous reactions of organic particles

196 Figure 3a illustrates the product distribution during the ozonolysis of Sqe aerosols. Consistent with prior observations (Liu et
197 al., 2024), maximum product yields were achieved at approximately 60% Sqe conversion (corresponding to 0.678 ppm O_3),
198 with representative products (SOZs, aldehydes, and acids) shown in Figs. S2 and S3. Figures 3b and S3 show representative
199 products from heterogeneous reactions between SOZs with ethylamine (C_2H_7N), with mass spectral analysis revealing three
200 product classes. First, protonated molecular ions (denoted as $[M+H]^+$) appear at m/z 314, 368, 382, 436, 450, 504, 558, 572,
201 626, 640, 694, and 762, corresponding to adducts from reactions between SOZs and ethylamine, i.e., SOZs + C_2H_7N . For
202 instance, the m/z 504 peak corresponds to $C_{32}H_{57}O_3N$ (*MW* 503) from the reaction of C_{30} SOZ ($C_{30}H_{50}O_3$) with C_2H_7N . Detailed
203 reaction mechanisms are discussed in Sect. 3.3. Second, the deprotonated ions ($[M-H]^-$) at m/z 294, 348, 362, 416, 430, and
204 484 derive from subsequent dehydration products from SOZs + C_2H_7N reactions, i.e., SOZs + $C_2H_7N - H_2O$. For instance, the
205 m/z 484 peak matches the H_2O loss product of $C_{32}H_{57}O_3N$, i.e., $C_{32}H_{57}O_3N - H_2O$. Third, the deprotonated ions ($[M-H]^-$) at
206 m/z 278, 332, 346, 400, 414, 468, and 536 correspond to the H_2O_2 elimination products from SOZs and C_2H_7N reactions, i.e.,
207 SOZs + $C_2H_7N - H_2O_2$. For instance, the m/z 468 peak represents the H_2O_2 elimination product of $C_{32}H_{57}O_3N$, i.e., $C_{32}H_{57}O_3N$
208 – H_2O_2 . Notably, dehydration and H_2O_2 elimination products were only observed for smaller SOZs ($C_n < 35$), suggesting that
209 substituent effects and chain length of SOZs could influence the amination reaction pathways (see Sect. 3.3 for mechanistic
210 details).

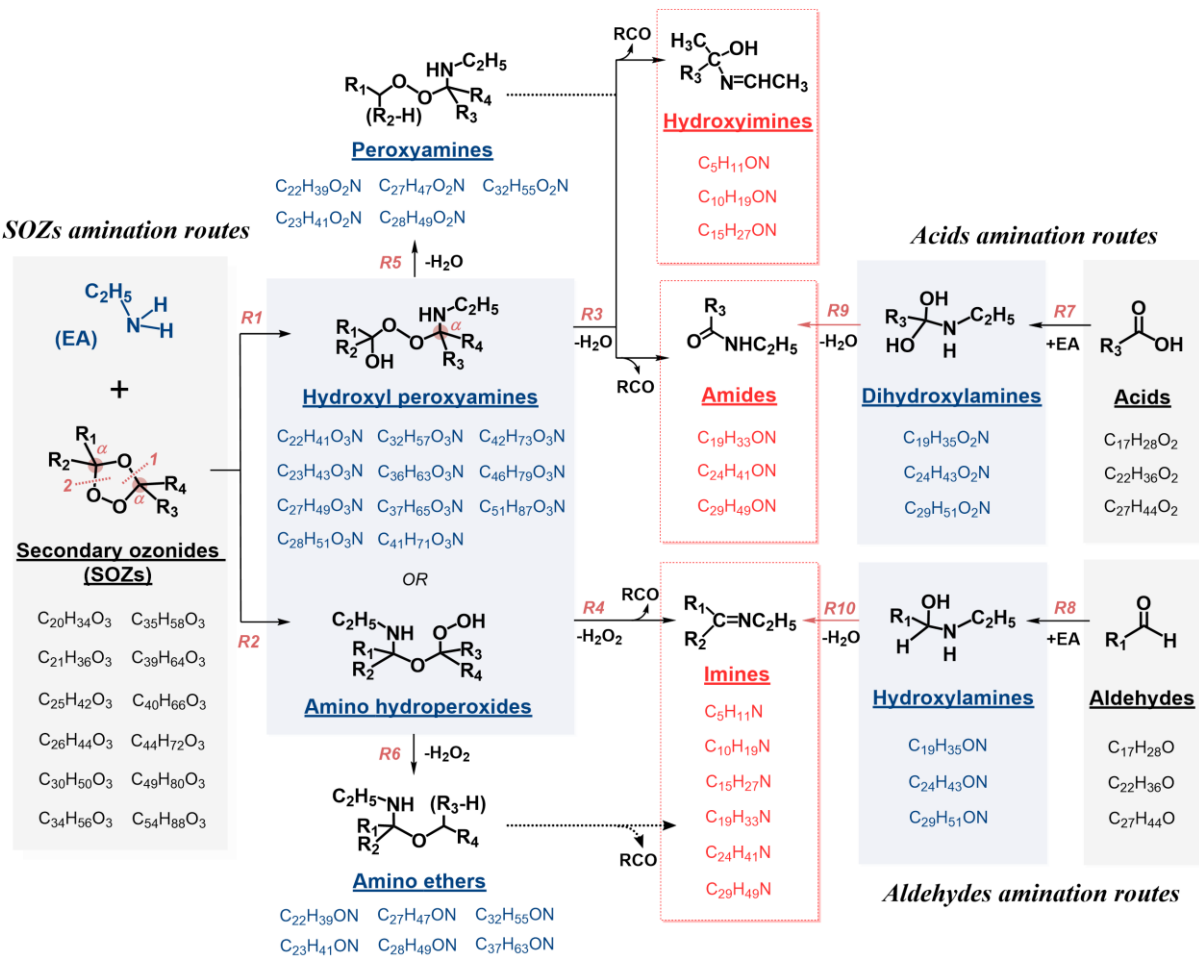


212 **Figure 3: Mass spectra of (a) representative SOZs formed during the ozonolysis of Sqe in the first flowtube reactor,**
 213 **and (b) their amination products (adducts of SOZ + EA are in red and dehydration products are in blue) upon exposure**
 214 **to ethylamine (EA) in the secondary flowtube reactor.**

215 Figures S2b and S3b illustrate the products formed from heterogeneous reactions of C_{17} , C_{22} , and C_{27} aldehydes (RCHOs), as
 216 well as C_{17} , C_{22} , and C_{27} carboxylic acids (RCOOHs) upon ethylamine exposure in the secondary flowtube reactor. The
 217 protonated molecular ions ($[M+H]^+$) at m/z 294, 310, 362, 378, 430, and 446 correspond to products from reactions of these
 218 aldehydes (or carboxylic acids) with ethylamine (C_2H_7N), i.e., RCHOs (or RCOOHs) + C_2H_7N (Bain et al., 2016; De Haan et
 219 al., 2011). For instance, the peak at m/z 294 is assigned to $C_{19}H_{35}ON$ (*MW* 293) formed from the reaction of C_{17} aldehyde
 220 ($C_{17}H_{28}O$) with C_2H_7N . These RCHOs (or RCOOHs) + C_2H_7N adducts subsequently undergo H_2O elimination reactions (Shen
 221 et al., 2023; Bain et al., 2016; De Haan et al., 2009; Tuguldurova et al., 2024), producing characteristic peaks at m/z 276, 344,
 222 and 412 (from aldehyde reactions); as well as m/z 292, 360, and 428 (from acid reactions). For instance, the $[M+H]^+$ peak at
 223 m/z 276 corresponds $C_{19}H_{33}N$ (*MW* 275), resulting from H_2O elimination from $C_{19}H_{35}ON$, i.e., $C_{19}H_{35}ON - H_2O$.

224 **3.3 Amination mechanisms of secondary ozonides, carboxylic acids, and aldehydes**

225 A reaction mechanism was developed to elucidate the heterogeneous reactions of organic aerosols, including SOZs, carboxylic
226 acids ($C_{17}H_{28}O_2$, $C_{22}H_{36}O_2$, and $C_{27}H_{44}O_2$), and aldehydes ($C_{17}H_{28}O$, $C_{22}H_{36}O$, and $C_{27}H_{44}O$).
227 For SOZs, the electronegativity of neighboring oxygen atoms induces a net positive charge on the α -carbon atoms (Fig. 4),
228 facilitating nucleophilic attack by an amine (Jørgensen and Gross, 2009). This could lead to the formation of either hydroxyl
229 peroxyamines (R1) or amino hydroperoxides (R2), depending on the nucleophilic attack sites (Zahardis et al., 2008; Jørgensen
230 and Gross, 2009; Almatarneh et al., 2020). However, these competing pathways and their proposed products remain
231 controversial (Fig. S11). Zahardis et al. (2008) proposed that SOZ reaction with octadecylamine generates a hydroxyl
232 peroxyamine intermediate, which subsequently decomposes to nonanal and a C_{27} amide via H_2O elimination (Fig. S11a).
233 Conversely, Almatarneh et al. (2020), Jørgensen and Gross (2009), and Na et al. (2006) suggested that SOZ reactions with
234 ammonia form amino hydroperoxide intermediates (Figs. S11b to S11e). Notably, neither hydroxyl peroxyamine nor amino
235 hydroperoxide intermediates have been experimentally detected in these studies (Zahardis et al., 2008; Almatarneh et al., 2020;
236 Jørgensen and Gross, 2009; Na et al., 2006). Contrasting both pathways, Qiu et al. (2024) demonstrated that ethylamine
237 addition to a cyclic SOZ directly yields a linear amination product through simultaneously H_2O elimination (Fig. S11a), i.e.,
238 bypassing formation of either proposed intermediates (Fig. S11f).



239

240 **Figure 4: Amination mechanisms of secondary ozonides (SOZs), carboxylic acids (RCOOHs), and aldehydes (RCHOs) upon**
 241 **ethylamine (EA) exposure, with representative chemical structures and compositions of reactants and products.**

242 In this work, mass peaks corresponding to SOZs + ethylamine ($\text{C}_2\text{H}_7\text{N}$) adducts were observed (Fig. 3b), providing direct
 243 experimental evidence for nucleophilic attack by ethylamine on SOZs. The MS^2 spectra provide complementary evidence for
 244 their structural characterization. Figure 5 illustrates representative MS^2 fragmentation patterns of the $[\text{C}_{32}\text{H}_{58}\text{O}_3\text{N}]^+$ ion
 245 (denoted as $[\text{M}+\text{H}]^+$), corresponding to the $\text{C}_{32}\text{H}_{57}\text{O}_3\text{N}$ product formed from C_{30} SOZ ($\text{C}_{30}\text{H}_{50}\text{O}_3$) + ethylamine ($\text{C}_2\text{H}_7\text{N}$)
 246 reaction. Two representative isomers, a hydroxyl peroxyamine (I) and amino hydroperoxide (II), were selected for analysis
 247 (Fig. 5a). Both isomers undergo $\text{C}_2\text{H}_5\text{NH}$ elimination, yielding $[\text{M}-\text{C}_2\text{H}_6\text{N}]^+$ ions (m/z 459). The hydroxyl peroxyamine isomer
 248 (I) subsequently loses $\text{C}_3\text{H}_7\text{O}$ and $\text{C}_{11}\text{H}_{18}$ to form m/z 294, while the amino hydroperoxide isomer (II) eliminates HO_2 yielding
 249 m/z 426. Additional fragmentation peaks (m/z 60, 86, 149, 383, and 441) may derive from these isomers. It is also noted that
 250 C_{30} SOZ isomers formation during the ozonolysis of Sqe (Figs. S9 and S10b) suggests additional $\text{C}_{32}\text{H}_{57}\text{O}_3\text{N}$ isomers likely
 251 contribute to these fragmentation patterns (Fig. 5). Figure 6a illustrates the kinetics of representative C_{30} hydroxyl
 252 peroxyamines (or amino hydroperoxides) as a function of ethylamine exposure.

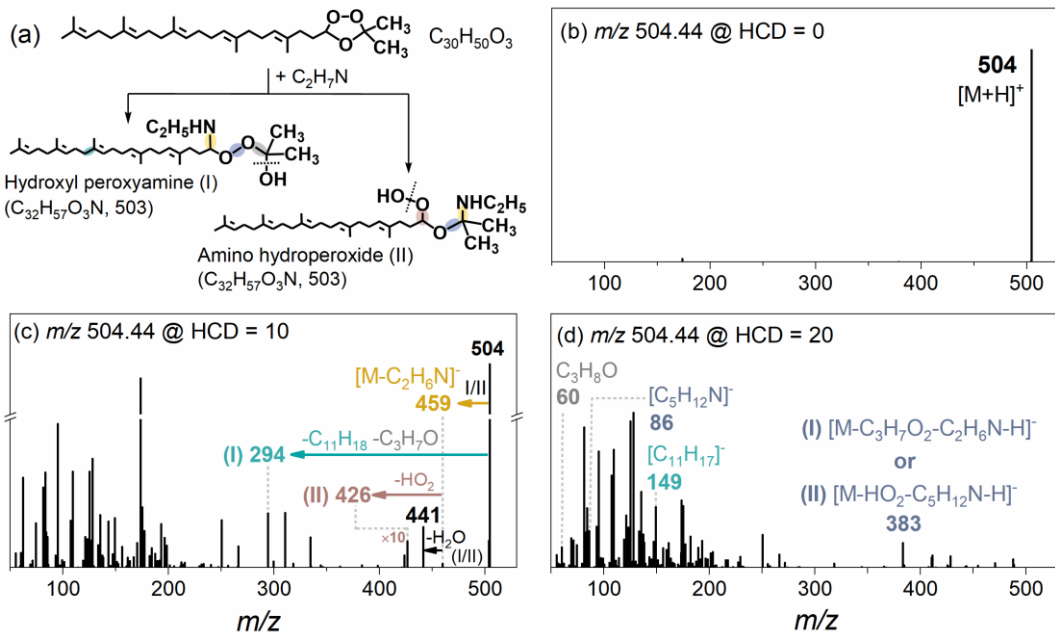
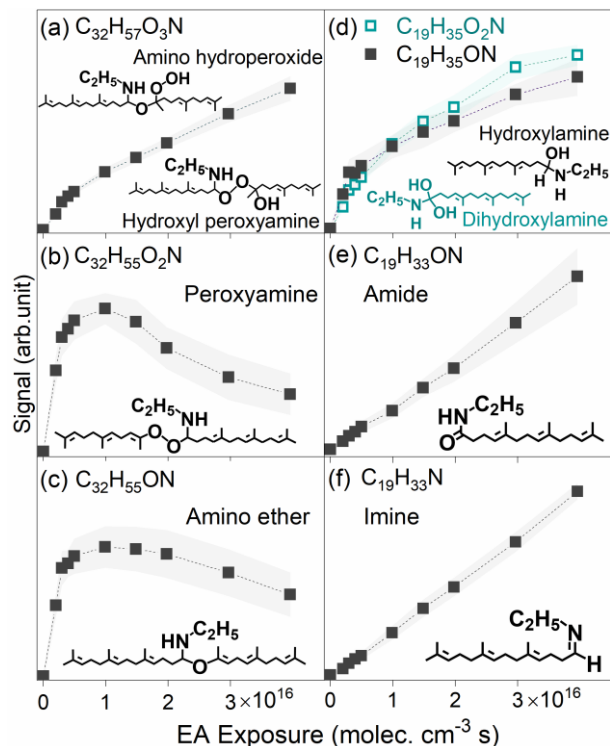


Figure 5: (a) Structures of two representative isomers ($C_{32}H_{57}O_3N$, MW 503), i.e., hydroxyl peroxyamine (I) and amino hydroperoxide (II). (b-d) MS^2 fragmentation of their protonated ions at HCD energies: (b) 0%, (c) 10%, and (d) 20 %.



257 **Figure 6: Experimental signal as a function of ethylamine (EA) exposure for: (a) hydroxyl peroxyamine (or amino hydroperoxide),**

258 (b) peroxyamine, (c) amino ether, (d) dihydroxylamine and hydroxylamine, (e) amide, and (f) imine.

259 Consumption reactions for the amino hydroperoxide and hydroxyl peroxyamine intermediates were previously proposed
260 (Zahardis et al., 2008; Na et al., 2006; Almatarneh et al., 2020; Jørgensen and Gross, 2009). Amino hydroperoxide
261 decomposition has been demonstrated to generate smaller imines and aldehydes via H₂O₂ elimination (Fig. 4). For instance,
262 Almatarneh et al. (2020) demonstrated that a C₂ amino hydroperoxide decomposition yields methylenimine, formaldehyde,
263 and H₂O₂ (Fig. S11). Consistently, products with compositions of C₅H₁₁N, C₁₀H₁₉N, C₁₅H₂₇N, C₁₉H₃₃N, C₂₄H₄₁N, and C₂₉H₄₉N
264 are assigned to be imines (Fig. S13) that could be attributed to these reactions. In contrast, for hydroxyl peroxyamine, Zahardis
265 et al. (2008) reported that hydroxyl peroxyamine decomposition generates a C₂₇ amide, C₉ aldehyde with H₂O elimination.
266 Observed products with compositions of C₁₉H₃₃ON, C₂₄H₄₁ON, and C₂₉H₄₉ON are proposed to be amides (Fig. S12) that could
267 be formed from these pathways. Moreover, hydroxyl peroxyamines lacking α -H atoms form hydroxyimines (C₅H₁₁ON,
268 C₁₀H₁₉ON, and C₁₅H₂₇ON), rather than amides. For instance, a C₃₆ hydroxyl peroxyamine with available α -H atom (Fig. S12a)
269 decomposes to a C₁₉ amide, C₁₇ aldehyde and H₂O, whereas a C₂₈ hydroxyl peroxyamine without α -H atom (Fig. S12b) yields
270 C₁₅ hydroxyimine, C₁₃ ketone, and H₂O.

271 These hydroxyimines, amides, and imines (Fig. 4) exhibit significantly lower carbon numbers than their precursor hydroxy
272 peroxyamines (R3) or amino hydroperoxides (R4). Consequently, neither R3 nor R4 pathways explain observed products
273 retaining same carbon numbers with amino hydroperoxides or hydroxy peroxyamines. This work therefore proposes two new
274 pathways: R5 (hydroxyl peroxyamine \rightarrow H₂O + peroxyamine), and R6 (amino hydroperoxide \rightarrow H₂O₂ + amino ether). With
275 C₃₂ intermediates for example, these pathways reasonably explain observed C₃₂H₅₅O₂N (peroxyamine) and C₃₂H₅₅ON (amino
276 ether) products formed from C₃₂H₅₇O₃N via H₂O or H₂O₂ elimination, respectively (Figs. 6b and 6c). The observed trend of
277 their experimental signal, which initially increased and then decreased as a function of ethylamine exposure, providing
278 evidence for mediating the conversion of hydroxy peroxyamine (or amino hydroperoxide) to hydroxylamine, amide, and imine.
279 Given the absence of these pathways in prior work (Almatarneh et al., 2020; Na et al., 2006; Zahardis et al., 2008; Qiu et al.,
280 2024; Jørgensen and Gross, 2009), these R5 and R6 require further investigations. Figure S15 summarizes a simplified
281 mechanism involving four key intermediates, including hydroxyl peroxyamines, peroxyamines, amino hydroperoxides, and
282 amino ethers.

283 Figure 4 illustrates reaction mechanisms for ethylamine reactions with C₁₇, C₂₂, and C₂₇ carboxylic acids, as well as C₁₇, C₂₂,
284 and C₂₇ aldehydes, forming dihydroxylamines (R7) and hydroxylamines (R8), respectively (De Haan et al., 2011; Ditto et al.,
285 2022; Bain et al., 2016; Shashikala et al., 2023; Sarkar et al., 2019). For instance, the nucleophilic attack reaction of ammonia
286 at carbonyl (C=O) site of acetaldehyde generates a hydroxylamine as demonstrated by Sarkar et al. (2019). Here,
287 dihydroxylamines (C₁₉H₃₅O₂N, C₂₄H₄₃O₂N, C₂₉H₅₁O₂N) and hydroxylamines (C₁₉H₃₅ON, C₂₄H₄₃ON, and C₂₉H₅₁ON) have
288 been measured by APPI-HRMS (Fig. S2b) (Sarkar et al., 2019), as well as their kinetics as a function of ethylamine exposure
289 (e.g., C₁₉ dihydroxylamine and hydroxylamine in Fig. 6d). Subsequent H₂O elimination reactions of dihydroxylamines and
290 hydroxylamines yield amides (R9, C₁₉H₃₃ON, C₂₄H₄₁ON, and C₂₉H₄₉ON) and imines (R10, e.g., C₁₉H₃₃N, C₂₄H₄₁N, and

291 C₂₉H₄₉N) (Montgomery and Day, 1965), respectively, as shown in Fig. S2b. For example, C₁₇ aldehyde (C₁₇H₂₈O, Fig. S14a)
292 reacts with ethylamine to generate C₁₉ hydroxylamine intermediate (C₁₉H₃₅ON, *MW* 293), which dehydrates to C₁₉ imine
293 (C₁₉H₃₃N, *MW* 275). Additionally, these amides and imines can be also produced from hydroxyl peroxyamines (R3) or amino
294 hydroperoxides (R4), as shown in Figs. 6e and 6f.

295 **4 Conclusions**

296 Atmospheric amines critically modulate the evolution of aerosols and particulate pollution. Here, we investigate heterogeneous
297 reactions of ethylamine with SOZs, carboxylic acids, and aldehydes aerosols using a tandem flowtube reactor combined with
298 online APPI-HRMS. Heterogeneous reactivities ($\Delta\gamma_{\text{eff}}$) for SOZs decrease 17.5-fold with increasing carbon chain length, from
299 $\Delta\gamma_{\text{eff}} = 1.0 \times 10^{-4}$ for C₂₁ SOZ to 5.7×10^{-6} for C₄₉ SOZ, with nonmonotonic behavior suggesting substitution effects. Crucially,
300 reactions of ethylamine with carboxylic acids and aldehydes exhibit $\Delta\gamma_{\text{eff}}$ values of 10^{-4} to 10^{-5} , exceeding SOZs reactivity at
301 equivalent carbon numbers, with reactivity similarly declining with chain length. This reactivity dependence implies
302 atmospheric lifetimes ($\tau \propto \gamma^{-1}$) spanning two orders of magnitude across these organic aerosols, thereby controlling their
303 differential impacts on air quality, health, and climate.

304 Moreover, hydroxyl peroxyamines, amino hydroperoxides, peroxyamines, and amino ethers, were measured as characteristic
305 intermediates linking SOZ consumption to stable nitrogenous products (hydroxyimines, amides, and imines).
306 Dihydroxylamines and hydroxylamines from reactions of carboxylic acids and aldehydes were characterized as crucial
307 intermediates. Further reaction mechanism analysis reveals that nucleophilic addition of ethylamine to SOZs initiates the
308 formation of hydroxyl peroxyamines and amino hydroperoxides. Beyond established cleavage pathways yielding form
309 hydroxyimines, amides, and imines, this work demonstrates new elimination pathways: hydroxyl peroxyamines (amino
310 hydroperoxides) \rightarrow H₂O (or H₂O₂) + peroxyamines (or amino ethers). These mechanistic insights elucidate the transformation
311 of organic aerosols to nitrogen-containing secondary organic aerosols (SOAs), providing fundamental parameters for more
312 accurate modeling of atmospheric processes.

313
314 **Data availability.** The authors confirm that the data supporting the findings of this work are available within the article and
315 its supplementary information.

316
317 **Supplement.** Supplementary details about the experimental data (Figs. S1 to S7) and reaction mechanism (Figs. S8 to S15,
318 and Tables S1 to S2).

319
320 **Author contributions.** PL performed the investigation, data curation, formal analysis, and wrote the original draft. JG and
321 YH contributed to data curation. WY, ZZ, and FQ conducted the methodology. MZ were responsible for conceptualization,
322 methodology, supervision, and reviewed and edited the manuscript.

323
324 **Competing interests.** The authors declare no competing financial interest.
325
326 **Acknowledgments.** The authors are grateful for the funding support from the National Natural Science Foundation of China
327 and Shanghai Science and Technology Innovation Action Plan. The authors thank Kevin R. Wilson (Lawrence Berkeley
328 National Laboratory) for helpful discussions.
329
330 **Financial support.** This study was supported by the National Natural Science Foundation of China (22373066, 52376119)
331 and Shanghai Science and Technology Innovation Action Plan (24142201500).

332 **References**

333 Almatarneh, M. H., Alrebei, S. F., Altarawneh, M., Zhao, Y., and Abu-Saleh, A. A.-A.: Computational study of the dissociation
334 reactions of secondary ozonide, *Atmosphere.*, 11, 100-110, <https://doi.org/10.3390/atmos11010100>, 2020.
335 Arata, C., Heine, N., Wang, N., Misztal, P. K., Wargocki, P., Bekö, G., Williams, J., Nazaroff, W. W., Wilson, K. R., and
336 Goldstein, A. H.: Heterogeneous ozonolysis of squalene: gas-phase products depend on water vapor concentration, *Environ.*
337 *Sci. Technol.*, 53, 14441-14448, <https://doi.org/10.1021/acs.est.9b05957>, 2019.
338 Bain, R. M., Pulliam, C. J., Ayrton, S. T., Bain, K., and Cooks, R. G.: Accelerated hydrazone formation in charged
339 microdroplets, *Rapid. Commun. Mass. Sp.*, 30, 1875-1878, <https://doi.org/10.1002/rcm.7664>, 2016.
340 Bos, S. J., van Leeuwen, S. M., and Karst, U.: From fundamentals to applications: recent developments in atmospheric pressure
341 photoionization mass spectrometry, *Anal. Bioanal. Chem.*, 384, 85-99, <https://doi.org/10.1007/s00216-005-0046-1>, 2006.
342 Charville, H., Jackson, D. A., Hodges, G., Whiting, A., and Wilson, M. R.: The uncatalyzed direct amide formation reaction -
343 mechanism studies and the key role of carboxylic acid H - bonding, *Eur. J. Org. Chem.*, 2011, 5981-5990,
344 <https://doi.org/10.1002/ejoc.201100714>, 2011.
345 De Haan, D. O., Tolbert, M. A., and Jimenez, J. L.: Atmospheric condensed-phase reactions of glyoxal with methylamine,
346 *Geophys. Res. Lett.*, 36, 11819-11823, <https://doi.org/10.1029/2009gl037441>, 2009.
347 De Haan, D. O., Hawkins, L. N., Kononenko, J. A., Turley, J. J., Corrigan, A. L., Tolbert, M. A., and Jimenez, J. L.: Formation
348 of nitrogen-containing oligomers by methylglyoxal and amines in simulated evaporating cloud droplets, *Environ. Sci. Technol.*,
349 45, 984-991, <https://doi.org/10.1021/es102933x>, 2011.
350 Ditto, J. C., Abbatt, J. P. D., and Chan, A. W. H.: Gas- and particle-phase amide emissions from cooking: mechanisms and air
351 quality impacts, *Environ. Sci. Technol.*, 56, 7741-7750, <https://doi.org/10.1021/acs.est.2c01409>, 2022.
352 Fairhurst, M. C., Ezell, M. J., and Finlayson-Pitts, B. J.: Knudsen cell studies of the uptake of gaseous ammonia and amines
353 onto C₃-C₇ solid dicarboxylic acids, *Phys. Chem. Chem. Phys.*, 19, 26296-26309, <https://doi.org/10.1039/c7cp05252a>, 2017a.

354 Fairhurst, M. C., Ezell, M. J., Kidd, C., Lakey, P. S. J., Shiraiwa, M., and Finlayson-Pitts, B. J.: Kinetics, mechanisms and
355 ionic liquids in the uptake of n-butylamine onto low molecular weight dicarboxylic acids, *Phys. Chem. Chem. Phys.*, 19, 4827-
356 4839, <https://doi.org/10.1039/c6cp08663b>, 2017b.

357 Fredenhagen, A. and Kuhnol, J.: Evaluation of the optimization space for atmospheric pressure photoionization (APPI) in
358 comparison with APCI, *J. Mass. Spectrom.*, 49, 727-736, <https://doi.org/10.1002/jms.3401>, 2014.

359 Gao, X., Zhang, Y., and Liu, Y.: A kinetics study of the heterogeneous reaction of n-butylamine with succinic acid using an
360 ATR-FTIR flow reactor, *Phys. Chem. Chem. Phys.*, 20, 15464-15472, <https://doi.org/10.1039/c8cp01914b>, 2018.

361 George, I. J. and Abbatt, J. P.: Heterogeneous oxidation of atmospheric aerosol particles by gas-phase radicals, *Nat. Chem.*, 2,
362 713-722, <https://doi.org/10.1038/nchem.806>, 2010.

363 Heine, N., Houle, F. A., and Wilson, K. R.: Connecting the elementary reaction pathways of criegee intermediates to the
364 chemical erosion of squalene interfaces during ozonolysis, *Environ. Sci. Technol.*, 51, 13740-13748,
365 <https://doi.org/10.1021/acs.est.7b04197>, 2017.

366 Hon, Y. S., Lin, S. W., Lu, L., and Chen, Y. J.: The mechanistic study and synthetic applications of the base treatment in the
367 ozonolytic reactions, *Tetrahedron.*, 51, 5019-5034, [https://doi.org/10.1016/0040-4020\(95\)98699-I](https://doi.org/10.1016/0040-4020(95)98699-I), 1995.

368 Jacobs, M. I., Xu, B., Kostko, O., Heine, N., Ahmed, M., and Wilson, K. R.: Probing the heterogeneous ozonolysis of squalene
369 nanoparticles by photoemission, *J. Phys. Chem. A.*, 120, 8645-8656, <https://doi.org/10.1021/acs.jpca.6b09061>, 2016.

370 Jørgensen, S. and Gross, A.: Theoretical investigation of reactions between ammonia and precursors from the ozonolysis of
371 ethene, *Chem. Phys.*, 362, 8-15, <https://doi.org/10.1016/j.chemphys.2009.05.020>, 2009.

372 Lee, D. and Wexler, A. S.: Atmospheric amines - part III: Photochemistry and toxicity, *Atmos. Environ.*, 71, 95-103,
373 <https://doi.org/10.1016/j.atmosenv.2013.01.058>, 2013.

374 Liu, P., Gao, J., Xiao, X., Yuan, W., Zhou, Z., Qi, F., and Zeng, M.: Investigating the kinetics of heterogeneous lipid ozonolysis
375 by an online photoionization high-resolution mass spectrometry technique, *Anal. Chem.*, 96, 19576-19584,
376 <https://doi.org/10.1021/acs.analchem.4c04404>, 2024.

377 Liu, Y., Ma, Q., and He, H.: Heterogeneous uptake of amines by citric acid and humic acid, *Environ. Sci. Technol.*, 46, 11112-
378 11118, <https://doi.org/10.1021/es302414v>, 2012.

379 Montgomery, M. W. and Day, E. A.: Aldehyde-amine condensation reaction: a possible fate of carbonyls in foods, *J. Food.*
380 *Sci.*, 30, 828-832, <https://doi.org/10.1111/j.1365-2621.1965.tb01849.x>, 1965.

381 Na, K., Song, C., and Cockerii, D.: Formation of secondary organic aerosol from the reaction of styrene with ozone in the
382 presence and absence of ammonia and water, *Atmos. Environ.*, 40, 1889-1900, <https://doi.org/10.1016/j.atmosenv.2005.10.063>,
383 2006.

384 Na, K., Song, C., Switzer, C., and Cocker, D. R.: Effect of ammonia on secondary organic aerosol formation from α -pinene
385 ozonolysis in dry and humid conditions, *Environ. Sci. Technol.*, 41, 6096-6102, <https://doi.org/10.1021/es061956y>, 2007.

386 Ponec, R., Yuzhakov, G., Haas, Y., and Samuni, U.: Theoretical analysis of the stereoselectivity in the ozonolysis of olefins.
387 Evidence for a modified criegee mechanism, *J. Org. Chem.*, 62, 2757-2762, <https://doi.org/10.1021/jo9621377>, 1997.

388 Qiu, J., Fujita, M., Tonokura, K., and Enami, S.: Stability of terpenoid-derived secondary ozonides in aqueous organic media,
389 *J. Phys. Chem. A.*, 126, 5386-5397, <https://doi.org/10.1021/acs.jpca.2c04077>, 2022.

390 Qiu, J., Shen, X., Chen, J., Li, G., and An, T.: A possible unaccounted source of nitrogen-containing compound formation in
391 aerosols: amines reacting with secondary ozonides, *Atmos. Chem. Phys.*, 24, 155-166, <https://doi.org/10.5194/acp-24-155-2024>, 2024.

393 Sarkar, S., Oram, B. K., and Bandyopadhyay, B.: Ammonolysis as an important loss process of acetaldehyde in the troposphere:
394 energetics and kinetics of water and formic acid catalyzed reactions, *Phys. Chem. Chem. Phys.*, 21, 16170-16179,
395 <https://doi.org/10.1039/c9cp01720h>, 2019.

396 Shashikala, K., Niha, P. M., Aswathi, J., Sharanya, J., and Janardanan, D.: Theoretical exploration of new particle formation
397 from glycol aldehyde in the atmosphere - A temperature-dependent study, *Comput. Theor. Chem.*, 1222, 114057-114067,
398 <https://doi.org/10.1016/j.comptc.2023.114057>, 2023.

399 Shen, X., Chen, J., Li, G., and An, T.: A new advance in the pollution profile, transformation process, and contribution to
400 aerosol formation and aging of atmospheric amines, *Environ. Sci.: Atmos.*, 3, 444-473, <https://doi.org/10.1039/d2ea00167e>,
401 2023.

402 Smith, J. D., Kroll, J. H., Cappa, C. D., Che, D. L., Liu, C. L., Ahmed, M., Leone, S. R., Worsnop, D. R., and Wilson, K. R.:
403 The heterogeneous reaction of hydroxyl radicals with sub-micron squalane particles: a model system for understanding the
404 oxidative aging of ambient aerosols, *Atmos. Chem. Phys.*, 9, 3209-3222, <https://doi.org/10.5194/acp-9-3209-2009>, 2009.

405 Smith, J. N., Barsanti, K. C., Friedli, H. R., Ehn, M., Kulmala, M., Collins, D. R., Scheckman, J. H., Williams, B. J., and
406 McMurry, P. H.: Observations of aminium salts in atmospheric nanoparticles and possible climatic implications, *Proc. Natl.
407 Acad. Sci. U. S. A.*, 107, 6634-6639, <https://doi.org/10.1073/pnas.0912127107>, 2010.

408 Tian, X., Chan, V. Y., and Chan, C. K.: Secondary organic aerosol formation from aqueous ethylamine oxidation mediated by
409 particulate nitrate photolysis, *ACS ES&T Air.*, 1, 951-959, <https://doi.org/10.1021/acs.estair.3c00095>, 2024.

410 Tuguldurova, V. P., Kotov, A. V., Vodyankina, O. V., and Fateev, A. V.: Nature or number of species in a transition state: the
411 key role of catalytically active molecules in hydrogen transfer stages in atmospheric aldehyde reactions, *Phys. Chem. Chem.
412 Phys.*, 26, 5693-5703, <https://doi.org/10.1039/d3cp04500e>, 2024.

413 Zahardis, J., Geddes, S., and Petrucci, G. A.: The ozonolysis of primary aliphatic amines in fine particles, *Atmos. Chem. Phys.*,
414 8, 1181-1194, <https://doi.org/10.5194/acp-8-1181-2008>, 2008.

415 Zahardis, J., LaFranchi, B. W., and Petrucci, G. A.: Photoelectron resonance capture ionization-aerosol mass spectrometry of
416 the ozonolysis products of oleic acid particles: Direct measure of higher molecular weight oxygenates, *J. Geophys. Res.: Atmo.*,
417 110, D08307, <https://doi.org/10.1029/2004jd005336>, 2005.

418 Zeng, M., Heine, N., and Wilson, K. R.: Evidence that criegee intermediates drive autoxidation in unsaturated lipids, Proc.
419 Natl. Acad. Sci. U. S. A., 117, 4486-4490, <https://doi.org/10.1073/pnas.1920765117>, 2020.